Journal of
Materials Chemistry A

PAPER

Cite this: *J. Mater. Chem. A*, 2019, **7**, 27603

Activating MoS_2 basal planes for hydrogen evolution through direct CVD morphology control†

Lianqing Dong,[a] Shaoqiang Guo,[a] Yuyan Wang,[a] Qinghua Zhang,[b] Lin Gu,[b] Caofeng Pan[c] and Junying Zhang*[a]

Monolayer MoS_2 has emerged as an active and non-precious electrocatalyst for electrochemical hydrogen production. The atomic thinness and ultrahigh surface-to-volume ratio of the chemical vapor deposition (CVD)-grown monolayers result in an ideal material to facilitate efficient electrochemical hydrogen evolution and explore the mechanism at the atomic level. However, the active sites of pristine monolayer MoS_2 are reported to locate at the edges, leaving the basal planes inert, which limits their hydrogen evolution reaction performance. Here, we synthesize monolayer MoS_2 hexagonal flakes with high surface coverage and abundant highly distributed S vacancies as active reaction sites directly by CVD. The catalytic performance of the hexagonal MoS_2 flakes presented here is superior to that of the existing as-grown MoS_2, exhibiting a current density of 100 mA cm^{-2} at −353 mV *versus* the reversible hydrogen electrode (RHE) with an extraordinarily low onset potential of only 41 mV. And an outstanding exchange current density of 0.091 mA cm^{-2} stands as the highest ever reported for all kinds of non-precious-metal doped MoS_2 catalysts. It is proved by a variety of tests that abundant S vacancies are distributed in the highly crystalline basal plane of hexagonal MoS_2, which leads to a remarkably improved catalytic efficiency compared with that of the triangular one. The monolayer MoS_2 is further evidenced to have excellent long-term stability and high durability, maintaining a stable performance for nine months in air and retaining the initial performance after 6000 cyclic voltammetry scans. On-site defect engineering of monolayer MoS_2 for excellent hydrogen evolution reaction (HER) performance enriches insights into the structure–performance relationship in 2D materials and provides new opportunities for the design of highly active catalysts.

Received 10th August 2019
Accepted 16th November 2019

DOI: 10.1039/c9ta08738a

rsc.li/materials-a

1. Introduction

MoS_2 stands out as one of the most attractive candidates for catalyzing the hydrogen evolution reaction (HER) process due to its low cost and excellent reaction activity.[1–3] Compared with conventional MoS_2-based particulate catalysts obtained *via* chemical exfoliation or hydrothermal routes, single layer MoS_2 prepared by chemical vapor deposition (CVD) can avoid the relatively low crystal quality, severe aggregation behaviour and poor electrical coupling to the electrode, which usually arise from nanoparticle and nanosheet samples.[4] Furthermore, monolayer MoS_2 catalysts show potential development prospects because the high surface-to-volume ratio provides abundant active sites for the catalytic reaction. Density functional theory (DFT) calculations indicate that the d band of monolayer MoS_2 shifts up 0.1 eV towards the Fermi level compared with that of bulk MoS_2, and the electronic effect caused by the single layer strengthens H adsorption.[5] Furthermore, the atomically thin and flat nature of monolayers makes it possible to explore the mechanism of catalytic reactions at the atomic level. It also provides a perfect platform to study active sites and introduce various treatments for increasing the HER catalytic activity, for example by growing porous MoS_2 monolayers[6] and forming surface decorations.[7]

The facile and economical CVD method enables us to achieve mass production of high-quality monolayer MoS_2 with different morphologies. It is generally believed that the catalytic activity of MoS_2 originates from its edges;[8–10] however, the performance of pristine monolayer MoS_2 is largely limited by the low density of active sites within its basal plane, which restricts the practical application of this material for the HER. Therefore, various kinds of treatments have been carried out to solve these problems.[11] One major strategy to improve the performance is increasing the number of edge sites by, for example, reducing the sample size, increasing the coverage,

---

[a] Key Laboratory of Micro-Nano Measurement, Manipulation and Physics (Ministry of Education), School of Physics, Beihang University, Beijing 100191, China. E-mail: zjy@buaa.edu.cn

[b] Beijing National Laboratory for Condensed Matter Physics, Institute of Physics, Chinese Academy of Sciences, Beijing 100190, China

[c] Beijing Institute of Nanoenergy and Nanosystems, Chinese Academy of Sciences, Beijing 100083, China

† Electronic supplementary information (ESI) available. See DOI: 10.1039/c9ta08738a

artificially creating more edges in the basal plane or synthesizing dendritic flakes.[9,12,13] Furthermore, some recent studies have demonstrated many other treatments to enhance the catalytic activity, for instance, intercalating small cations (H^+ or Li^+) between the monolayers and the underlying substrates and controlling the crystalline structures.[14,15] Phase engineering and boundary activation have also been developed to overcome the limited catalytic activity of the MoS_2 basal plane.[16–18] However, most of the treatments are complicated and the performance should be further improved.

Recently, theoretical and experimental results have shown that the S-vacancies are catalytic sites, where gap states around the Fermi level allow hydrogen to bind directly to exposed Mo atoms.[19] So a pioneering strategy has been proposed involving the introduction of defects into the pristine MoS_2 plane, for instance, using heavy ion irradiation, oxygen plasma or hydrogen treatment to introduce more active sites.[20,21] However, post-treatment methods are not suitable for large-scale synthesis, and these methods may cause instability in fragile 2D materials such as inducing an unfavourable crystalline structure by plasma treatment.[22] It has also been demonstrated that the catalytic activity of S vacancies strongly depends on their appropriate density as well as the crystallinity.[22] The calculated optimal concentration of S vacancies for hydrogen adsorption is in the range of 12.5–15.62% and the S vacancies show better catalytic activities in higher-crystalline-quality MoS_2 according to previous reports.[22,23] Therefore, there is an urgent need for an *in situ* mass growth method of high-crystallinity 2D materials with tailored inherent defect concentrations to achieve high catalytic activity.

Here, we discuss the morphology-dependent properties of monolayer MoS_2 flakes obtained by the CVD method. It is evidenced that S vacancies with an ideal concentration of about 13.5% are formed in the CVD-grown hexagonal MoS_2. The HER performance of hexagonal flakes has been greatly improved compared with that of triangular ones with the same size and coverage, which have a smaller concentration of S vacancies. We also demonstrate that the S vacancies mainly contribute to the improvement of catalytic activity by comparing the catalytic activity before and after modifying the S vacancies. The HER performance exceeds that of the post-treatment samples, with a current density of 100 mA cm^{-2} at −353 mV *versus* the reversible hydrogen electrode (RHE), a Tafel slope of 53 mV per decade, an onset potential of 41 mV, and an ultrahigh exchange current density of 0.091 mA cm^{-2}.

2. Results and discussion

Monolayer MoS_2 flakes with different sizes and morphologies are synthesized by the CVD method under the conditions of a semi-closed environment developed by our group,[24] and then they are transferred onto glassy carbon substrates for catalytic characterization. The morphology and the size can be precisely controlled by adjusting the parameters. Specifically, 1 mg MoO_3 and 15 mg sulfur powder are placed in a 2.5 cm-diameter sealed quartz tube with a 4 mm-diameter air vent on the tube wall. Then the quartz tube is placed in a tube furnace with a 50 cm-diameter quartz tube (Fig. S1†). Triangular and hexagonal MoS_2 flakes can be obtained when the temperatures of the reaction area are 1000 °C and 850 °C, respectively. The edge lengths of

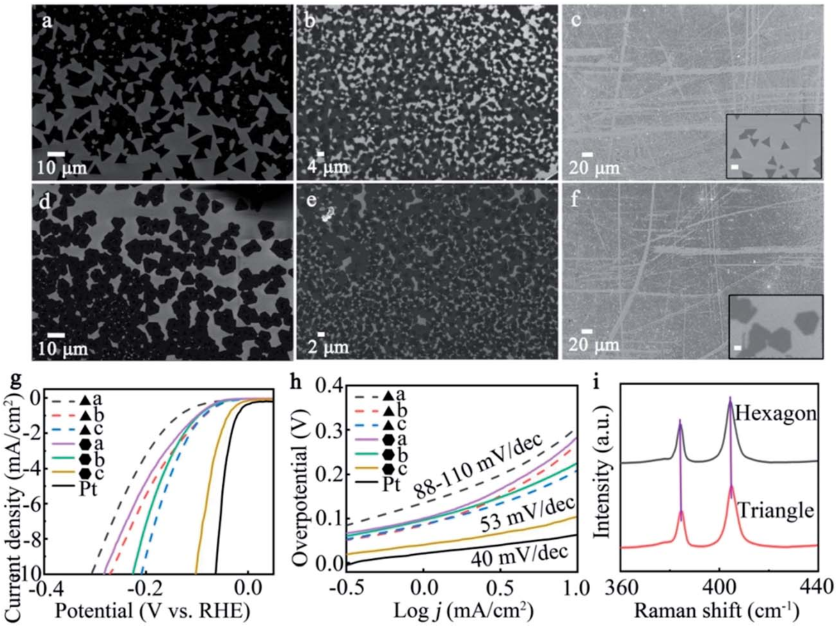

Fig. 1 HER activity of the as-grown MoS_2 flakes on Si/SiO_2. (a–f) SEM images of monolayer MoS_2 flakes on Si/SiO_2 with different morphologies and sizes. (a) Triangle a: triangular flakes with edge lengths less than 10 μm. (b) Triangle b: triangular flakes with edge lengths less than 5 μm. (c) Triangle c: triangular flakes with edge lengths less than 500 nm. (d) Hexagon a: hexagonal flakes with edge lengths less than 10 μm. (e) Hexagon b: hexagonal flakes with edge lengths less than 5 μm. (f) Hexagon c: hexagonal flakes with edge lengths less than 500 nm. The scale in the enlarged image is 200 nm. (g) Polarization curves of monolayer MoS_2 flakes with different morphologies and sizes. The polarization curve of Pt is also given as a reference. (h) Tafel plots of monolayer MoS_2 flakes. (i) Raman spectra of the triangular and hexagonal monolayers.

the MoS_2 flakes can be further controlled by precisely adjusting the reaction time. Scanning electron microscope (SEM) micrographs are then obtained to show the as-grown MoS_2 on Si/SiO_2 (Fig. 1(a)–(f) and S2†). It can be seen that the synthesized triangular and hexagonal MoS_2 flakes have a uniform size and the same surface coverage, mainly benefiting from the appropriate position of the substrate and our unique semi-closed growth method. Unlike in the single-tube CVD method with a continuous flow of Ar gas, which leads to sample growth downstream, most of the precursors react and quickly generate MoS_2 on the substrates above the ceramic boat in the semi-closed environment. This method allows the precursors to be fully utilized, which ensures coverage and reduces environmental pollution. As expected, every sample has similar MoS_2 surface coverage.

The HER activities of MoS_2 transferred onto glassy carbon are reflected in the polarization curves in Fig. 1(g). Interestingly, the hexagonal sample with the shortest edge length (hexagon c) possesses the best catalytic activity, and the overpotential (η) needed is only 104 mV to achieve a current density of 10 mA cm^{-2}, which is much smaller compared with that of the other five samples (209 mV, 225 mV, 268 mV, 282 mV and 307 mV for triangle c, hexagon b, triangle b, hexagon a and triangle a, respectively). Hexagon c has the lowest onset potential of 41 mV, which stands out as the lowest compared with previous reported CVD grown MoS_2 catalysts.[9,13,17] Hexagon c also possesses the lowest Tafel slope of 53 mV dec^{-1} (Fig. 1(h)), in comparison to the 88–110 mV dec^{-1} for the other samples. The exchange current density j_0, as another parameter for the HER rate, can be extrapolated according to the Tafel plots. Sample triangle c exhibits a j_0 of 0.038 mA cm^{-2}, which is comparable to the previous reports on samples with high coverage triangular flakes.[9] Surprisingly, sample hexagon c exhibits a remarkable j_0 of 0.091 mA cm^{-2}, which, as far as we know, is the highest value among those reported for CVD-grown monolayer MoS_2 catalysts (Fig. S3†). Electrochemical impedance spectroscopy (EIS) analysis of sample hexagon c and triangle c is also carried out and the results show an obvious decrease of charge-transfer impedance from the triangle to the hexagon (Fig. S4†).

HER performance tests indicate the significant regularity with which the catalytic performance increases with size reduction, and the catalytic performance of hexagons with the same size is always better than that of triangles. Raman spectra are obtained to probe the crystal quality and layer thickness, as shown in Fig. 1(i). The Raman spectra of the as-grown hexagonal and triangular flakes remain the same with respect to their relative intensity and peak position. The frequency difference between the out-of-plane vibration of S atoms (A_{1g}) and in-plane vibration of Mo and S atoms ($E_{2g}{}^1$) is $\Delta \sim 20$ cm^{-1}, which is in good agreement with that for the reported monolayer MoS_2 with good crystallinity.[25,26] Atomic force microscopy (AFM) of the triangular and hexagonal flakes is also performed to observe the strict monolayers (Fig. S5†). High uniformity of the triangular and hexagonal samples can also be verified from the integrated intensity maps of Raman vibration modes (Fig. S6†), which show that both the triangular and hexagonal monolayers are highly crystallized.

Considering that the edges of monolayer flakes always provide active sites for the HER,[10] a dendritic monolayer MoS_2 sample is further prepared as a comparison. The dendritic monolayer samples are synthesized by the same method at a higher temperature of 1050 °C for 15 min, and then they are completely transferred to the glassy carbon substrate (Fig. S7†). Three samples with triangular, dendritic and hexagonal monolayer flakes which have a similar size and coverage are selected, as shown in Fig. 2. As expected, the dendritic sample shows a lower overpotential required to achieve a current density of 10 mA cm^{-2} than the triangular sample, which is mainly because of the abundant edges.[13] However, the hexagonal sample presents a surprising character of its overpotential being much lower than that of the dendritic one. This result shows that the hexagonal flakes may have more active sites beyond the edges.

The hexagon shape of monolayer MoS_2 is formed with slightly different morphologies such as rounded hexagons, regular hexagons, scalene hexagons and shrinking triangles. To compare the difference of the in-plane crystal quality for different morphologies, an analysis of photoluminescence (PL) spectra at different morphologies is performed. Fig. 3 shows the normalized PL intensity maps of the as-grown samples in the shape of rounded hexagons with smooth edges (Fig. 3(a)), regular hexagons (Fig. 3(b)), scalene hexagons (Fig. 3(c)), shrinking triangles (Fig. 3(d)), triangles (Fig. 3(e)), and polygons (Fig. 3(f)). The PL emission of the rounded hexagon sample is concentrated and uniform in the plane, while the regular hexagon presents photoluminescence segmentation. The scalene hexagon sample also shows photoluminescence segmentation and the intensity of the central luminescence decreases. The maximum emission position locates at the edges in the shrinking triangles, while for the standard triangle, the maximum emission position moves towards the vertices. Usually, the emission positions in polygons are mainly along the edges. Note that PL intensity can indicate the general location of S vacancies in monolayer flakes.[27] The S vacancy is a type of electron-donating defect, leading to the formation of negatively charged excitons (also named negative trions). The test is performed under STP conditions, and it is found that S

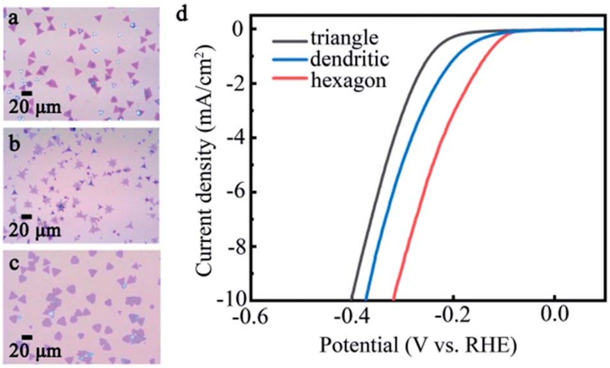

Fig. 2 Optical images of monolayer (a) triangular, (b) dendritic, and (c) hexagonal MoS_2. (d) The corresponding polarization curves.

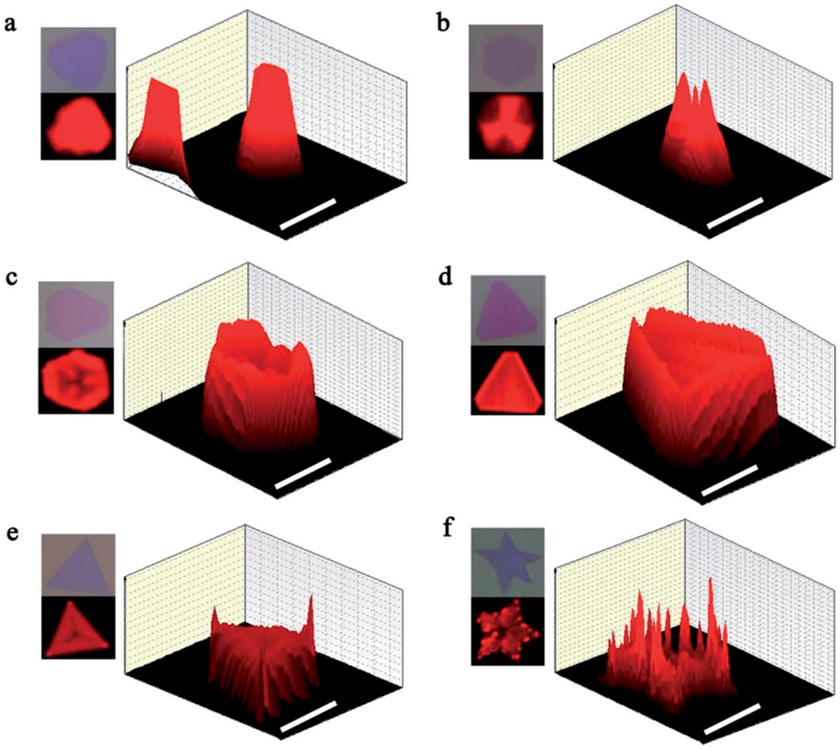

Fig. 3 Normalized PL intensity distribution of (a) rounded hexagons (with smooth edges), (b) regular hexagons, (c) scalene hexagons, (d) shrinking triangles, (e) triangles, and (f) polygons. The white scale is 2 μm.

vacancies can adsorb O_2 and H_2O and localize free electrons or trions to inhibit nonradiative recombination.[27–29] Based on this, the PL intensity intuitively demonstrates the concentration and distribution of S vacancies. It is confirmed that the hexagonal monolayer flakes always possess a higher density of S vacancies than the triangular ones because of the rich in-plane defects. The rotational symmetric growth of hexagonal flakes may result in abundant S vacancies. The MoS_2 crystals with polygonal

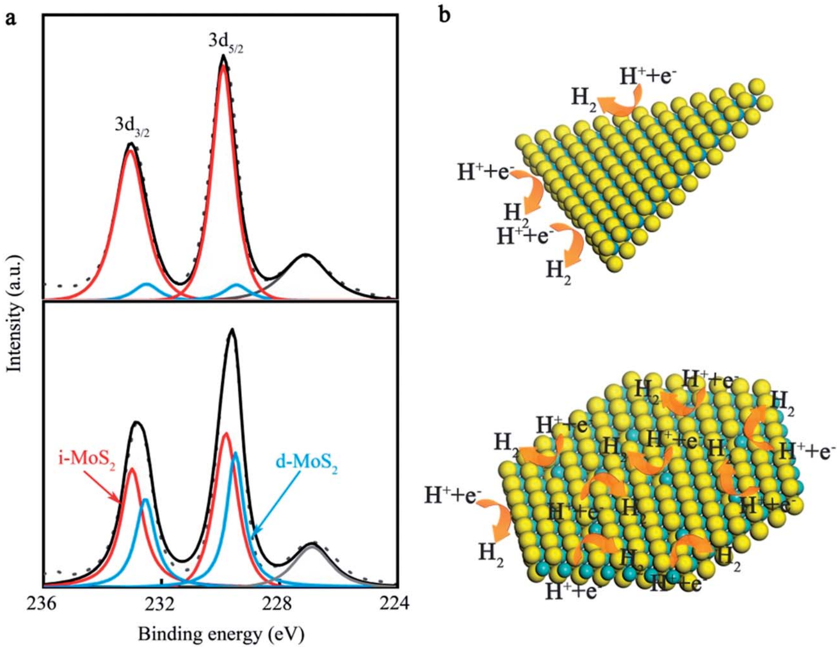

Fig. 4 (a) XPS results for Mo 3d of triangle and hexagon dominated films. Red lines represent the intrinsic MoS_2 and blue lines represent the defective MoS_2. (b) Schematic diagram of monolayer hexagonal and triangular MoS_2 flakes, which illustrates the edges and in-plane defects that work as the active catalytic sites for the HER.

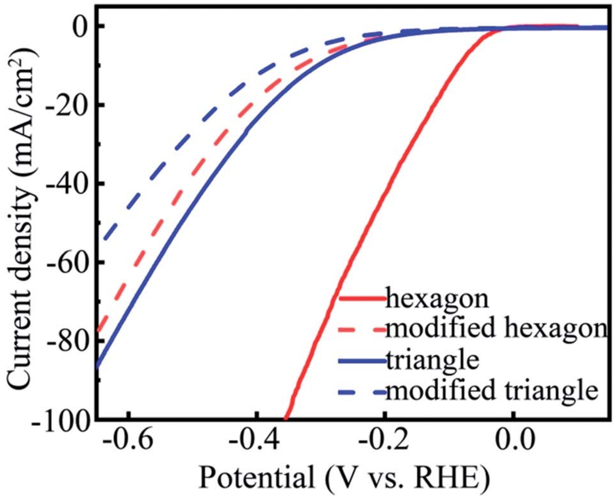

Fig. 5 Polarization curves of triangular and hexagonal flakes before (solid lines) and after (dotted lines) modification of S vacancies.

shapes usually involve twin crystal growth, especially for the highly symmetric hexagonal MoS_2, which forms a cyclic twin.[29,30] The mirror boundaries induced by the rotational growth further show 8-4-4 defects, which are molybdenum rich. As a result, abundant S vacancies are formed around the mirror boundaries in hexagonal MoS_2 crystals.[29,30] Meanwhile, structural imperfections may also play major roles in the spatial distribution of defects in most hexagonal flakes and may be caused during the CVD cooling process.[31] Therefore, the unique structure of the hexagons results in the concentration of defects in the plane.

X-ray photoelectron spectroscopy (XPS) is also performed to identify the S vacancies existing in the hexagonal flakes (Fig. 4(a)). The Mo 3d spectra consist of two sets of peaks that can be respectively assigned to intrinsic MoS_2 (i-MoS_2) and defective MoS_2 (d-MoS_2).[32] Mo^{4+} $3d_{5/2}$ and Mo^{4+} $3d_{3/2}$ peaks can be deconvoluted into i-MoS_2 (located at 229.92 eV and 233.07 eV) and d-MoS_2 (located at 229.47 eV and 232.52 eV). According to this result, there are more S vacancies in hexagonal flakes than in triangular flakes. The concentration of S vacancies in hexagonal flakes is estimated to be about 13.5%, which falls in the optimal S-vacancy concentration for the HER according to previous calculations.[23] Abundant sulfur defects can be visually observed in the hexagonal flakes using aberration-corrected annular dark-field scanning transmission electron microscopy (ADF-STEM, Fig. S8†). As shown in the schematic diagram, the abundant intrinsic S vacancies provide highly distributed active sites in the whole basal plane in hexagonal monolayer flakes without destroying the crystallinity, which is the key factor needed to improve the catalytic activity.

In order to further confirm the role of S vacancies in electrocatalytic hydrogen production, we tried to modify the S vacancies in different samples. We treated the samples with a poly (3,4-ethylenedioxythiophene:poly(styrenesulfonate)) (PEDOT:PSS) solution, which can heal the S vacancies.[32] Briefly, samples are immersed in the PEDOT:PSS solution for 15 min, followed by immersion in deionized (DI) water for 10 min. Then the S vacancies are healed spontaneously by sulfur adatom clusters on the MoS_2 surface through a PSS-induced hydrogenation process.[32] Both the triangular and hexagonal samples show an obvious decrease in their catalytic activity, as shown in Fig. 5, further evidencing the significant role of S vacancies in improving the performance of the hexagonal sample.

The sample with the smallest hexagonal monolayer MoS_2 flakes is used to test the durability. The SEM image of the as-grown monolayer hexagonal particles on SiO_2/Si is shown in Fig. 6(a) and the SEM image of monolayer hexagonal particles after cyclic voltammetry (CV) scans on glassy carbon is shown in Fig. 6(b). It can be seen that the morphology does not change after transfer and the cycling test. To achieve a current density of 10 mA cm^{-2}, an overpotential of 105 mV is needed, which is comparable to that of the materials that contain noble metals.[33–35] There is a slight improvement from the 1st to the 3000th cycle with a scan rate of 5 mV s^{-1}, which might be due to the intercalation of protons reported previously.[14] After this the performance is stable from the 3000th to the 6000th cycle

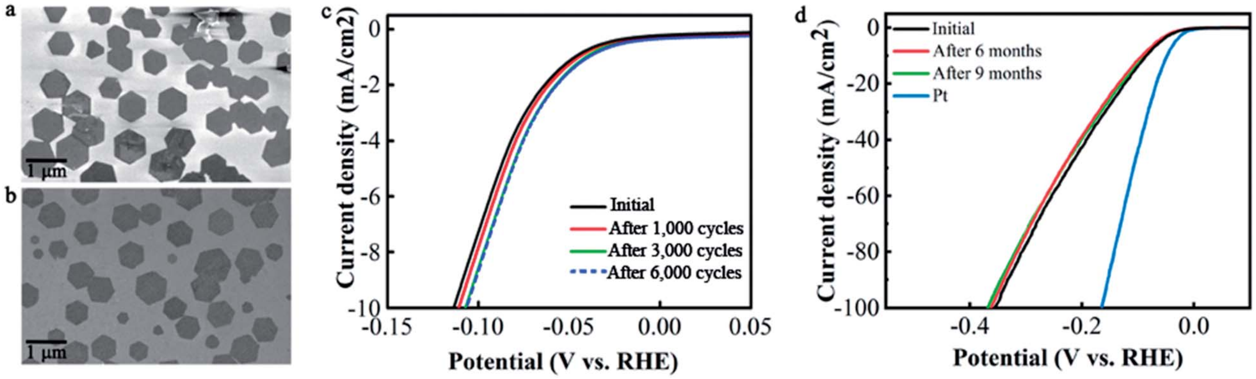

Fig. 6 Durability and stability test results of the CVD-grown hexagonal MoS_2 catalyst. (a) SEM image of the as-grown monolayer hexagonal particles on SiO_2/Si. (b) SEM image of monolayer hexagonal particles after the durability test on glassy carbon. (c) Polarization curves for the 1st, 1000th, 3000th, and 6000th cycle. (d) Polarization curves of the hexagonal MoS_2 flakes for the initial one and after 6 months and 9 months exposure to air, respectively.

Table 1 Comparison of HER performance for different CVD-grown monolayer MoS_2 samples

Materials	Tafel slope (mV cm^{-2})	η^a (mV *vs.* RHE)	$j_0{}^b$ (mA cm^{-2})	Onset potential (mV)	Ref.
MoS_2 (on an Au substrate)	61–74	−300 (−60 mA cm^{-2})	0.0381	−100	Shi *et al.*[9]
MoS_2 (defect engineered)	171/147	−680 (−20 mA cm^{-2}); ∼−575 (−6 mA cm^{-2})			Ye *et al.*[21]
MoS_2 (dendritic)	73	−300 (−40 mA cm^{-2})	0.0245	−100	Zhang *et al.*[13]
MoS_2 (nanopore patterning)	109	−500 (−100 mA cm^{-2})	0.0028		Su *et al.*[12]
MoS_2 (defect engineered)	50.3	−110 (−40 mA cm^{-2}); −67 (−10 mA cm^{-2})			He *et al.*[20]
MoS_2 (edge engineered)	55–60	∼−170 (−0.36 A cm^{-2})	0.0079		Jaramillo *et al.*[10]
MoS_2 (H^+ activation)	90.8	∼−250 (−20 mA cm^{-2})	0.015		Li *et al.*[14]
MoS_2 (control of the crystalline structure)	40	∼−170 (−20 mA cm^{-2})	0.0035		Li *et al.*[15]
MoS_2 (boundary activated)	73	−200 (−78 mA cm^{-2})	0.057	−100	Zhu *et al.*[17]
Sulfur-deficient MoS_2	53	−353 (−100 mA cm^{-2})	0.091	−41	This work

[a] Overpotential at an HER current density of *x* mA cm^{-2}. [b] Exchange current density.

(Fig. 6(c)). And the sample shows superior long-term stability, and a negligible difference can be observed after exposure to air for six and nine months (Fig. 6(d)). This again proves the high crystallinity and the structural stability of the CVD-grown MoS_2 monolayer. Moreover, XPS tests before and after 1000 CV scans were carried to show that the stoichiometry of S and Mo remains constant, which indicates that no change occurs in the number of S vacancies during the cycling process (Fig. S9†). This proves that the initial as-grown active sites determine the catalytic activity. The HER process in our work might follow the Volmer–Tafel mechanism, by which the intermediate hydrogen is adsorbed on the active sites, accepting other intermediate hydrogens to generate H_2(S1).

Table 1 summarizes the relevant literature regarding different treatment methods for MoS_2 catalysts and the corresponding electrocatalytic performance parameters (Tafel slope, overpotential, exchange current density and onset potential). The Tafel slope of the hexagonal monolayer is 53 mV dec^{-1}, surpassing most of the previous reported Tafel slopes for post-treatment MoS_2. And the hexagonal MoS_2 exhibits the lowest overpotential for the HER. In terms of the HER exchange current density, the hexagonal MoS_2 is the most active material among the as-grown catalysts. Furthermore, our sample exhibits an extremely small onset potential, much smaller than that in previous reports. The high electrode kinetic metrics discussed above highlight the exceptional H_2 evolution efficiency of hexagonal MoS_2.

We then perform DFT calculations on monolayer MoS_2 systems with different S vacancy concentrations. The band structures of monolayer MoS_2 systems with different S vacancy concentrations are shown in Fig. 7 (the position configuration of two S vacancies is shown in Fig. S10 and Table S1†). The zero energy point is set to the Fermi level in pure monolayer MoS_2, and the systems with S vacancies are corrected by aligning the vacuum potentials of these systems.[36] After introducing S vacancies into MoS_2, local energy levels are formed (the blue

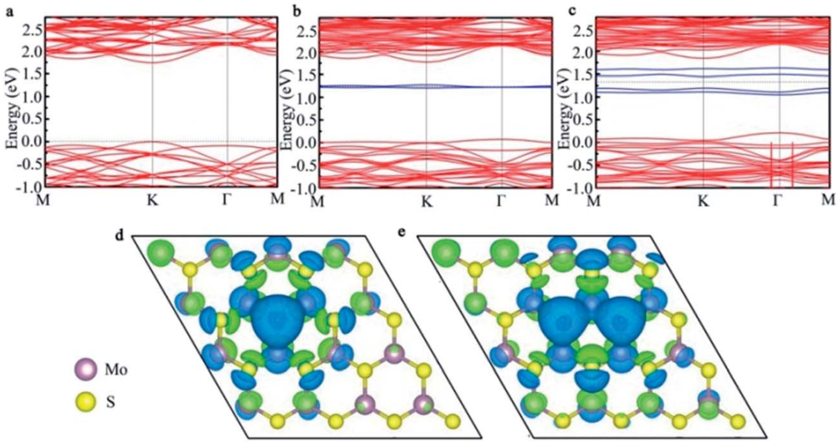

Fig. 7 Calculated band structures of monolayer MoS_2 with (a) no S vacancies, (b) one S vacancy, and (c) two S vacancies. The dotted lines indicate the Fermi levels. Corresponding charge density differences of monolayer MoS_2 with (d) one S vacancy and (e) two S vacancies. The green (deep blue) region indicates the charge accumulation (depletion), and the isosurface level is 0.02 electrons per $Bohr^3$.

lines in Fig. 7(b) and (c)). The Fermi level is raised into the localized energy state, showing the typical characters of an n-type semiconductor. The charge density difference is analyzed after introducing S vacancies into MoS_2 as shown in Fig. 7(d) and (e). Charges are depleted around S vacancies, indicating that extra electrons form after introducing S vacancies. The extra charge carriers induced by S vacancies occupy the lower conduction band states because of thermal activation at room temperature, leading to an increase of the electrical conductivity. Therefore, abundant S vacancies not only increase the number of active sites, but also enhance the intrinsic conductivity of MoS_2 catalysts due to the internal defect levels,[37] thus improving the catalytic activity.

3. Conclusions

In summary, we have proposed an effective approach to activate the inert basal planes of MoS_2 *via* the formation of intrinsic sulfur defects. The sulfur-deficient and nanosized monolayer hexagonal MoS_2 flakes synthesized by CVD are demonstrated to be potential electrocatalysts for the HER, and a low Tafel slope (53 mV dec^{-1}) and an outstanding high exchange current density of 0.091 mA cm^{-2} are achieved. The investigation into catalytically active sites in hexagonal MoS_2 sheds light on the design of high-performance 2D catalysts through morphology engineering. High electrode kinetic metrics as well as the excellent durability and stability highlight the superior H_2 evolution efficiency of hexagonal MoS_2. Intrinsic engineering of sulfur defects could provide a facile and effective route to enhance the catalytic performance of MoS_2 for hydrogen evolution, which is also inspiring for further applications through morphology engineering.

4. Experimental and computational details

4.1 MoS_2 growth and transfer

The monolayer MoS_2 flakes are grown on the 280 nm SiO_2/Si substrates in a semi-closed environment.[24] The furnace used here is a mini tube furnace with only one heating zone. The precursors used here are 1 mg molybdenum trioxide (MoO_3, 99.95% Alfa Aesar) and 15 mg sulfur (S, 99.99%, Alfa Aesar). Monolayer MoS_2 flakes are synthesized under atmospheric pressure using argon as the carrier gas. Precursors are placed in a quartz tube with a tiny hole on the tube wall. The distance between two precursors is 15 cm. WO_3 and the substrates are placed at the center of the heating zone. Before heating, the tube furnace is flushed three times with argon gas. The heating rate is maintained at 20 °C min^{-1}. Growth is carried out at temperatures of 1100 °C, 1000 °C and 850 °C for different morphologies. The holding time is 3 min, 6 min, and 9 min, respectively, for the different sizes.

The as-grown sample is first spin-coated with polymethyl methacrylate (PMMA) resists (AR-P 679.04) at 3000 rpm for 60 s. Then the sample is placed in a supersaturated KOH solution in a water bath at 50 °C until the PMMA/MoS_2 film is thoroughly separated from the substrate. Then the film is cleaned in DI water three times for 30 min each. For electrochemical characterization, the PMMA/MoS_2 is transferred onto 1 cm^2 glassy carbon. Then the sample is baked at 90 °C for 15 min to improve sample adhesion. Finally, the glassy carbon is placed in acetone solution for 30 min to remove PMMA.

For ADF-STEM sample preparation, the PMMA/MoS_2 is transferred onto Quantifoil grids and left to dry overnight in air. Then the sample is baked at 150 °C for 15 min to improve sample adhesion. Finally, the substrate is placed in an acetone solution for 5 min to remove PMMA.

4.2 Characterization of the samples

Raman and PL mapping are performed *via* an Andor 500i spectrograph with a 532 nm laser and a power of 1 mW. The Raman curves are obtained using a 1800 line per mm grating for 10 s, while PL maps are obtained with a 600 line per mm grating. XPS (PHI Quantera SXM, Japan, ULVAC-PHI) is used to characterize the defects. The size and shape of the samples are observed on an optical microscope and a field emission scanning electron microscope (Zeiss Merlin Compact) operating at 5 kV. AFM (Bruker, Dimension) is adopted to show the hexagonal and triangular flakes with a single layer. ADF-STEM imaging is conducted using a JEM-ARM200F.

4.3 Electrochemical characterization

Electrochemical measurements are performed in 0.5 M H_2SO_4 with a standard three-electrode configuration using an electrochemical analyzer (model CHI660E) with a carbon rod counter electrode and a Ag/AgCl electrode as the reference. MoS_2 flakes are transferred onto 1 cm^2 glassy carbon as the working electrode. Nitrogen gas is bubbled into the electrolyte throughout the experiment. Electrochemical characterization of the samples is performed using linear sweep voltammetry with a scan rate of 5 mV s^{-1} in 0.5 M H_2SO_4, $E(\mathrm{RHE}) = E(\mathrm{Ag/AgCl}) + 0.186$ V. The ac impedance is measured within the frequency range from 100 kHz to 0.01 Hz with a perturbation voltage amplitude of 5 mV.

4.4 Modification of S vacancies

A PEDOT:PSS solution is purchased from Macklin (1.5 wt%). The MoS_2 sample is immersed into the PEDOT:PSS solution for 15 min and then rinsed with DI water for 10 min. Finally, the substrate is blow-dried with nitrogen.

4.5 DFT calculations

To investigate the electronic properties of monolayer MoS_2 with one and two S vacancies, spin-polarized DFT calculations are performed by implementing the VASP code with the projector augmented wave (PAW) potential.[38,39] Exchange correlation energies are taken into account using the generalized gradient approximation using the Perdew–Burke–Ernzerhof (GGA-PBE) functional.[40] The kinetic energy cutoff of the plane wave expansion of the wave functions is set to 450 eV. To avoid spurious interaction between the periodic images, a minimum vacuum of 15 Å between two WS_2 layers is adopted. For the Brillouin zone sampling, a $9 \times 9 \times 1$ *k*-point mesh is employed in $4 \times 4 \times 1$ supercells. Gaussian smearing with a width of 0.03 eV is used around the Fermi surface. For structure optimization, the plane wave energy and the maximum tolerance of force are set as 1.0×10^{-4} eV and 0.01 eV Å^{-1}, respectively. Based on the above parameters, we calculate the band structures and charge density differences.

Conflicts of interest

There are no conflicts to declare.

Acknowledgements

This project was financially supported by the National Natural Science Foundation of China under Grant No. 51672016 and 51601006. This work was carried out at the National Supercomputing Center in Tianjin, and the calculations were performed on TianHe-1(A).

Notes and references

1 C. R. Zhu, D. Q. Gao, J. Ding, D. L. Chao and J. Wang, *Chem. Soc. Rev.*, 2018, **47**, 4332–4356.

2 A. B. Laursen, S. Kegnaes, S. Dahl and I. Chorkendorff, *Energy Environ. Sci.*, 2012, **5**, 5577–5591.

3 R. Wang, J. Han, X. Zhang and B. Song, *J. Mater. Chem. A*, 2018, **6**, 21847–21858.

4 M. Hong, J. Shi, Y. Huan, Q. Xie and Y. Zhang, *Nano Res.*, 2019, 1–10.

5 M.-R. Gao, M. K. Y. Chan and Y. Sun, *Nat. Commun.*, 2015, **6**, 7493.

6 Y. Yin, J. Han, Y. Zhang, X. Zhang, P. Xu, Q. Yuan, L. Samad, X. Wang, Y. Wang, Z. Zhang, P. Zhang, X. Cao, B. Song and S. Jin, *J. Am. Chem. Soc.*, 2016, **138**, 7965–7972.

7 Q. Ding, K. J. Czech, Y. Zhao, J. Zhai, R. J. Hamers, J. C. Wright and S. Jin, *ACS Appl. Mater. Interfaces*, 2017, **9**, 12734–12742.

8 C. L. Bentley, M. Kang, F. M. Maddar, F. Li, M. Walker, J. Zhang and P. R. Unwin, *Chem. Sci.*, 2017, **8**, 6583–6593.

9 J. Shi, D. Ma, G.-F. Han, Y. Zhang, Q. Ji, T. Gao, J. Sun, X. Song, C. Li, Y. Zhang, X.-Y. Lang, Y. Zhang and Z. Liu, *ACS Nano*, 2014, **8**, 10196–10204.

10 T. F. Jaramillo, K. P. Jørgensen, J. Bonde, J. H. Nielsen, S. Horch and I. Chorkendorff, *Science*, 2007, **317**, 100–102.

11 Q. Ji, Y. Zhang, J. Shi, J. Sun, Y. Zhang and Z. Liu, *Adv. Mater.*, 2016, **28**, 6207–6212.

12 S. Su, Q. Zhou, Z. Zeng, D. Hu, X. Wang, M. Jin, X. Gao, R. Nötzel, G. Zhou, Z. Zhang and J. Liu, *ACS Appl. Mater. Interfaces*, 2018, **10**, 8026–8035.

13 Y. Zhang, Q. Ji, G.-F. Han, J. Ju, J. Shi, D. Ma, J. Sun, Y. Zhang, M. Li, X.-L. Lang, Y. Zhang and Z. Liu, *ACS Nano*, 2014, **8**, 8617–8624.

14 G. Li, D. Zhang, Y. Yu, S. Huang, W. Yang and L. Cao, *J. Am. Chem. Soc.*, 2017, **139**, 16194–16200.

15 Y. Li, Y. Yu, Y. Huang, R. A. Nielsen, W. A. Goddard III, Y. Li and L. Cao, *ACS Catal.*, 2014, **5**, 448–455.

16 L. Liu, J. Wu, L. Wu, M. Ye, X. Liu, Q. Wang, S. Hou, P. Lu, L. Sun, J. Zheng, L. Xing, L. Gu, X. Jiang, L. Xie and L. Jiao, *Nat. Mater.*, 2018, **17**, 1108–1114.

17 J. Zhu, Z.-C. Wang, H. Dai, Q. Wang, R. Yang, H. Yu, M. Liao, J. Zhang, W. Chen, Z. Wei, N. Li, L. Du, D. Shi, W. Wang, L. Zhang, Y. Jiang and G. Zhang, *Nat. Commun.*, 2019, **10**, 1348.

18 Y. Yu, G.-H. Nam, Q. He, X.-J. Wu, K. Zhang, Z. Yang, J. Chen, Q. Ma, M. Zhao, Z. Liu, F.-R. Ran, X. Wang, H. Li, X. Huang, B. Li, Q. Xiong, Q. Zhang, Z. Liu, L. Gu, Y. Du, W. Huang and H. Zhang, *Nat. Chem.*, 2018, **10**, 638–643.

19 H. Li, C. Tsai, A. L. Koh, L. Cai, A. W. Contryman, A. H. Fragapane, J. Zhao, H. S. Han, H. C. Manoharan, F. Abild-Pedersen, J. K. Nørskov and X. Zheng, *Nat. Mater.*, 2016, **15**, 48–53.

20 Z. He, R. Zhao, X. Chen, H. Chen, Y. Zhu, H. Su, S. Huang, J. Xue, J. Dai, S. Cheng, M. Liu, X. Wang and Y. Chen, *ACS Appl. Mater. Interfaces*, 2018, **10**, 42524–42533.

21 G. Ye, Y. Gong, J. Lin, B. Li, Y. He, S. T. Pantelides, W. Zhou, R. Vajtai and P. M. Ajayan, *Nano Lett.*, 2016, **16**, 1097–1103.

22 G. Li, D. Zhang, Q. Qiao, Y. Yu, D. Peterson, A. Zafer, R. Kumar, S. Curtarolo, F. Hunte, S. Shannon, Y. Zhu, W. Yang and L. Cao, *J. Am. Chem. Soc.*, 2016, **138**, 16632–16638.

23 C. Tsai, H. Li, S. Park, J. Park, H. S. Han, J. K. Nørskov, X. Zheng and F. Abild-Pedersen, *Nat. Commun.*, 2017, **8**, 15113.

24 L. Dong, Y. Wang, J. Sun, C. Pan, Q. Zhang, L. Gu, B. Wan, C. Song, F. Pan, C. Wang, Z. Tang and J. Zhang, *2D Mater.*, 2018, **6**, 015007.

25 V. K. Kumar, S. Dhar, T. H. Choudhury, S. A. Shivashankar and S. Raghavan, *Nanoscale*, 2015, **7**, 7802–7810.

26 X. Yang, Q. Li, G. Hu, Z. Wang, Z. Yang, X. Liu, M. Dong and C. Pan, *Sci. China Mater.*, 2016, **59**, 182–190.

27 H. Nan, Z. Wang, W. Wang, Z. Liang, Y. Lu, Q. Chen, D. He, P. Tan, F. Miao, X. Wang, J. Wang and Z. Ni, *ACS Nano*, 2014, **8**, 5738–5745.

28 S. Tongay, J. Zhou, C. Ataca, J. Liu, J. S. Kang, T. S. Matthews, L. You, J. Li, J. C. Grossman and J. Wu, *Nano Lett.*, 2013, **13**, 2831–2836.

29 G. Zhang, J. Wang, Z. Wu, R. Shi, W. Ouyang, A. Amini, B. N. Chandrashekar, N. Wang and C. Cheng, *ACS Appl. Mater. Interfaces*, 2016, **9**, 763–770.

30 A. M. van der Zande, P. Y. Huang, D. A. Chenet, T. C. Berkelbach, Y. You, G.-H. Lee, T. F. Heinz, D. R. Reichman, D. A. Muller and J. C. Hone, *Nat. Mater.*, 2013, **12**, 554.

31 Y. Sheng, X. Wang, K. Fujisawa, S. Ying, A. L. Elias, Z. Lin, W. Xu, Y. Zhou, A. M. Korsunsky, H. Bhaskaran, M. Terrones and J. H. Warner, *ACS Appl. Mater. Interfaces*, 2017, **9**, 15005–15014.

32 X. Zhang, Q. Liao, S. Liu, Z. Kang, Z. Zhang, J. Du, F. Li, S. Zhang, J. Xiao, B. Liu, Y. Ou, X. Liu, L. Gu and Y. Zhang, *Nat. Commun.*, 2017, **8**, 15881.

33 M. Chhetri, U. Gupta, L. Yadgarov, R. Rosentsveig, R. Tenne and C. N. R. Rao, *Dalton Trans.*, 2015, **44**, 16399–16404.

34 J. Deng, H. Li, J. Xiao, Y. Tu, D. Deng, H. Yang, H. Tian, J. Li, P. Ren and X. Bao, *Energy Environ. Sci.*, 2015, **8**, 1594–1601.

35 Y. Shi, J. Wang, C. Wang, T.-T. Zhai, W.-J. Bao, J.-J. Xu, X.-H. Xia and H.-Y. Chen, *J. Am. Chem. Soc.*, 2015, **137**, 7365–7370.

36 P. G. Moses and C. G. Van de Walle, *Appl. Phys. Lett.*, 2010, **96**, 021908.

37 L. Lin, N. Miao, Y. Wen, S. Zhang, P. Ghosez, Z. Sun and D. A. Allwood, *ACS Nano*, 2016, **10**, 8929–8937.

38 G. Kresse and J. Furthmüller, *Phys. Rev. B: Condens. Matter Mater. Phys.*, 1996, **54**, 11169.

39 G. Kresse and D. Joubert, *Phys. Rev. B: Condens. Matter Mater. Phys.*, 1999, **59**, 1758.

40 J. P. Perdew, K. Burke and M. Ernzerhof, *Phys. Rev. Lett.*, 1996, **77**, 3865.